Toroidal Dipole-Enhanced Third Harmonic Generation of Deep Ultraviolet Light using Plasmonic Meta-Atoms

Arash Ahmadivand,[†,‡] Michael Semmlinger,[†,‡] Liangliang Dong,[#,‡] Burak Gerislioglu,[⊥,‡] Peter Nordlander,[⊥,†,‡] and Naomi J. Halas[□,⊥,†,⊥,‡]

⊥Department of Physics and Astronomy, †Department of Electrical and Computer Engineering, #Department of Chemistry, ‡Laboratory for Nanophotonics, Rice University, 6100 Main Street, Houston, Texas 77005, United States

Abstract

The harmonic generation of light with plasmonic and all-dielectric nanostructures has gained much recent interest. This approach is especially promising for short wavelength (i.e. ultraviolet (UV)) generation, where conventional nonlinear crystals reach their limits both in transparency and in their ability to achieve phase-matching between the input and output fields. Here we demonstrate that the third harmonic generation of deep UV light in an indium tin oxide (ITO) film can be substantially enhanced by a metasurface consisting of metallic toroidal meta-atoms covered with an alumina layer for protection against laser induced damage. This approach combines the benefits of the large nonlinear susceptibility of ITO with the unique field enhancement properties of a toroidal metasurface. This ITO-meta-atom combination produces a third harmonic signal at a wavelength of 262 nm that is nominally 5 times larger than that of an ITO film patterned with a conventional hotspot-enhanced plasmonic dimer array. This result demonstrates the potential for toroidal meta-atoms as the active engineered element in a new generation of enhanced nonlinear optical materials and devices.

KEYWORDS: third harmonic generation, metamaterial, toroidal resonance, deep-ultraviolet light, indium tin oxide

Introduction

The conversion of multiple low-energy photons into a single high-energy photon, known as harmonic generation, has been employed extensively for decades both for fundamental optics and for its numerous applications. These include nonlinear sensors,[1] nanorulers,[2] bioimaging enhancement,[3] lasers,[4–6] and light harvesters.[7] The generation of optical harmonics also finds frequent application in the development of commercial laser tools.[8] In particular, third harmonic generation (THG) has been demonstrated successfully in dielectric metasurfaces,[9-11] plasmonic subwavelength platforms,[12-14] metallodielectric Fano clusters[15], and atomically thin monolayers.[8,16] One advantage of THG, compared to second harmonic generation, is that it does not require a nonlinear medium that lacks inversion symmetry.[17] Since the nonlinear signal generated increases with the third power of the incident electromagnetic field intensity, the corresponding conversion efficiency can be increased substantially by maximizing the excitation density.[18] Plasmonic nanostructures have become increasingly popular nanophotonic systems for nonlinear optics due to their ability to strongly localize an incident electromagnetic field at metallodielectric interfaces.[19] Strongly-coupled nanoparticle clusters[15,20,21] and well-engineered artificial planar and 3D meta-atoms[7] are examples of typical subwavelength platforms for the excitation of nonlinear features in, and by, plasmonic structures. In particular, ITO-plasmonic hybrid systems have shown to enhance THG compared to bare plasmonic structures[22-24].

Structures known as non-radiating anapoles have recently been introduced for producing ultrastrong nonlinear features in both metallodielectric and all-dielectric systems; they have been used to demonstrate the generation of visible signals from near-infrared fundamental beams.[17,25,26] Anapoles originate from the destructive interference of toroidal and electric dipoles, and have head-to-tail charge-current configuration signatures. While anapoles provide strong nonlinear enhancements, exciting these modes at short wavelengths has been challenging, limiting their application for harmonic generation at short wavelengths. However, toroidal dipoles with charge-current configurations analogous to anapoles can be excited at shorter wavelengths (i.e. visible) and show strong electromagnetic field localization. They represent

volumetric oscillations of radial current $\vec{\boldsymbol{J}}$ (that is $\hat{\boldsymbol{r}} \cdot \vec{\boldsymbol{J}} \neq \mathbf{0}$) and therefore are fundamentally distinct from electric multipoles (oscillating charge density) or magnetic multipoles (oscillating transverse current $\vec{\boldsymbol{J}}$, that is $\hat{\boldsymbol{r}} \times \vec{\boldsymbol{J}} \neq \mathbf{0}$).[27] Generally, the projected far-field radiation pattern from a toroidal scatterer is largely concealed by classical electromagnetic multipoles.[17,25–28] Hence, the detection of such an inherently weak multipole requires well-engineered metamolecules or meta-atoms.

Here we report the generation of deep ultraviolet (DUV) light based on THG using a toroidal-resonant plasmonic metasurface. (The DUV is typically defined as the UV wavelength range shorter than 350 nm) The metasurface was fabricated on top of a substrate consisting of a thin indium tin oxide (ITO) layer on glass. An alumina layer was deposited on top of the metasurface to prevent it from being easily damaged by the pump laser beam. Taking advantage of the strong third-order susceptibility ($\chi^{(3)}$) of the ITO sublayer,[29] the toroidal metasurface was specifically designed to boost its THG signal from a fundamental beam at a wavelength of 785 nm, generating 262 nm UV light. To evaluate the benefits of this unique plasmonic metasurface for THG, we performed both numerical and experimental studies to compare the THG strength to that of a resonant dimer array. This comparison provides a valuable understanding of the superior nonlinear optical response of toroidal metasurfaces for UV light generation.

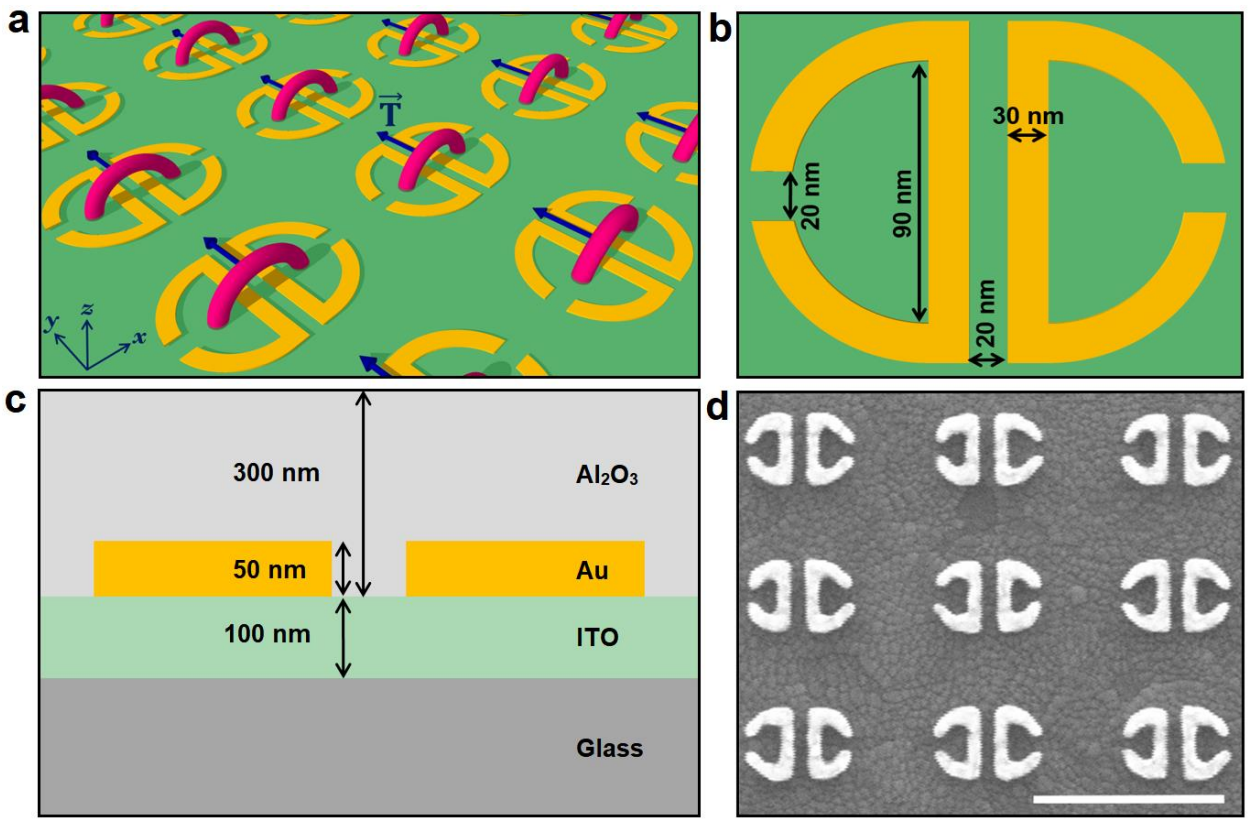

Figure 1. Design of the nonlinear plasmonic toroidal metasurface device. (a) General schematic of the metasurface design, showing the direction of the induced toroidal dipole moment and the formation of charge-current configurations between proximal resonators. (b) Top-view schematic of a single unit cell with geometric parameters. (c) Cross-sectional profile of the device. (d) SEM image of the toroidal metasurface prior to alumina deposition. Scale bar: 400 nm.

Results

The metasurface was fabricated as a two-dimensional periodic array of gold nanostructures on an ITO/glass substrate using electron-beam lithography. A schematic of the metasurface design shows the formation of closed-loop charge-current configurations between the proximal resonators within a unit cell, corresponding to the toroidal dipolar mode ($\overrightarrow{\boldsymbol{T}}$) (Figure 1a). The geometric parameters of the toroidal meta-atom are shown in Figure 1b. The period was selected to be 395 and 310 nm in the x and y directions, respectively, to maximize field enhancement (see Figure S1). A cross-sectional schematic of the unit cell is demonstrated in Figure 1c. The underlying 100 nm ITO layer serves as the nonlinear material, while the nanoresonators provide field enhancement to boost the THG. The plasmonic nanostructures are 50 nm thick and are covered with a 300 nm thick alumina capping layer to prevent deformation under intense laser

exposure. Finally, Figure 1d shows a representative scanning electron microscopy (SEM) image of the fabricated nanoarray with good uniformity prior to alumina deposition.

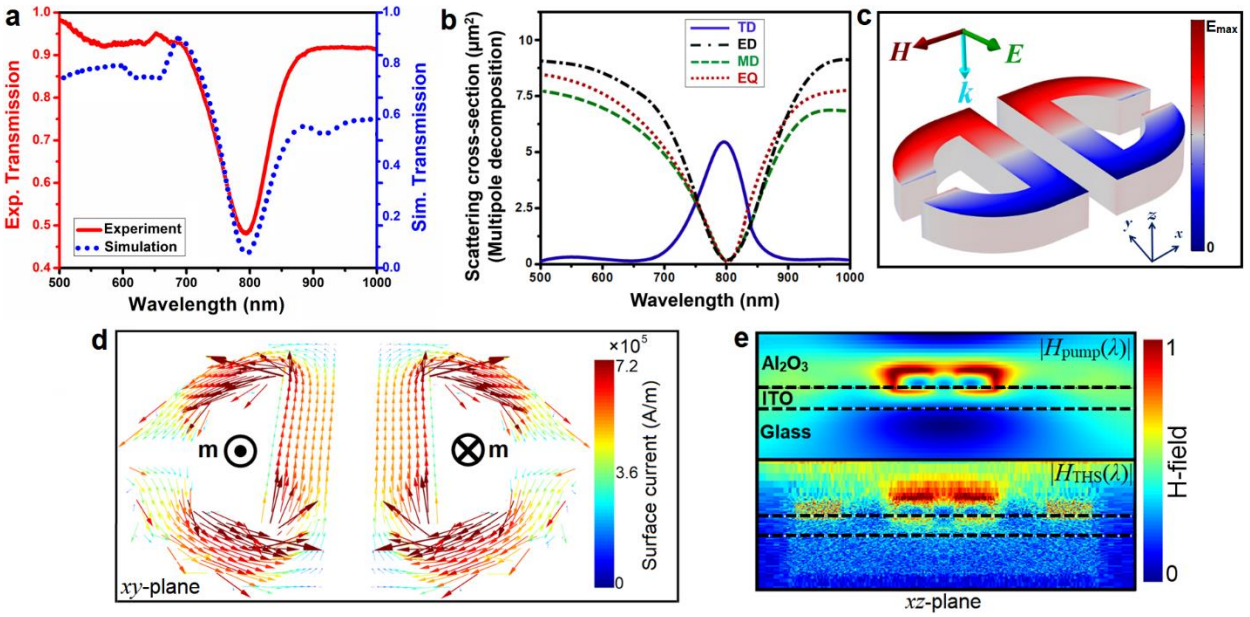

Figure 2. Sample characterization and numerical simulations. (a) Experimental (solid) and simulated (dotted) transmission spectrum of the toroidal metasurface. (b) Theoretical calculations of the scattering cross-sections of several multipoles present under illumination: TD, toroidal dipole; ED, electric dipole; MD, magnetic dipole; EQ, electric quadrupole. (c) Charge distribution on the top surface at the resonance frequency. (d) Vectorial surface current density map for the toroidal mode at the resonance frequency (top view). (e) Normalized magnetic field distribution at the fundamental ($|H_{pump}(\lambda)|$) and THG ($|H_{THG}(\lambda)|$) wavelengths (cross-sectional view).

Excitation with polarized light along the y-axis of the unit cells generates an optical resonance close to the excitation wavelength of 785 nm (Figure 2a). The simulated transmission spectrum shows good consistency with the experimental profile, while the discrepancy most likely originates from slight geometric differences between the fabricated and designed structures. To better understand the resonance properties, a detailed multipolar decomposition was performed using finite-difference time-domain simulations (FDTD, see Methods). The total scattering cross-section of the toroidal metasurface can be decomposed into contributions from a toroidal dipole (TD), an electric dipole (ED), a magnetic dipole (MD), and an electric quadrupole (EQ) (higher orders of the multipolar expansion were neglected in the computations). The dominant mode near the fundamental frequency can be attributed to the TD mode (Figure 2b). The charge distribution for the formation of the toroidal dipole, obtained using the finite-element method, is

shown in Figure 2c (FEM, see Methods). The corresponding electric field enhancement is provided in Figure S2. The electric field is highly confined in the two capacitive openings on both sides, producing antiparallel magnetic fields in neighboring resonators. This mismatch between induced magnetic moments is essential for the formation of the desired charge-current configuration across the unit cell. The mismatch in the numerically calculated induced surface current density vectorial profile is explicitly illustrated in Figure 2d (for details, see Methods). This loop current generates a significantly localized rotating magnetic field that penetrates deep into the ITO layer, shown as cross-sectional profiles at both the fundamental (top) and the third harmonic (bottom) wavelengths (Figure 2e).

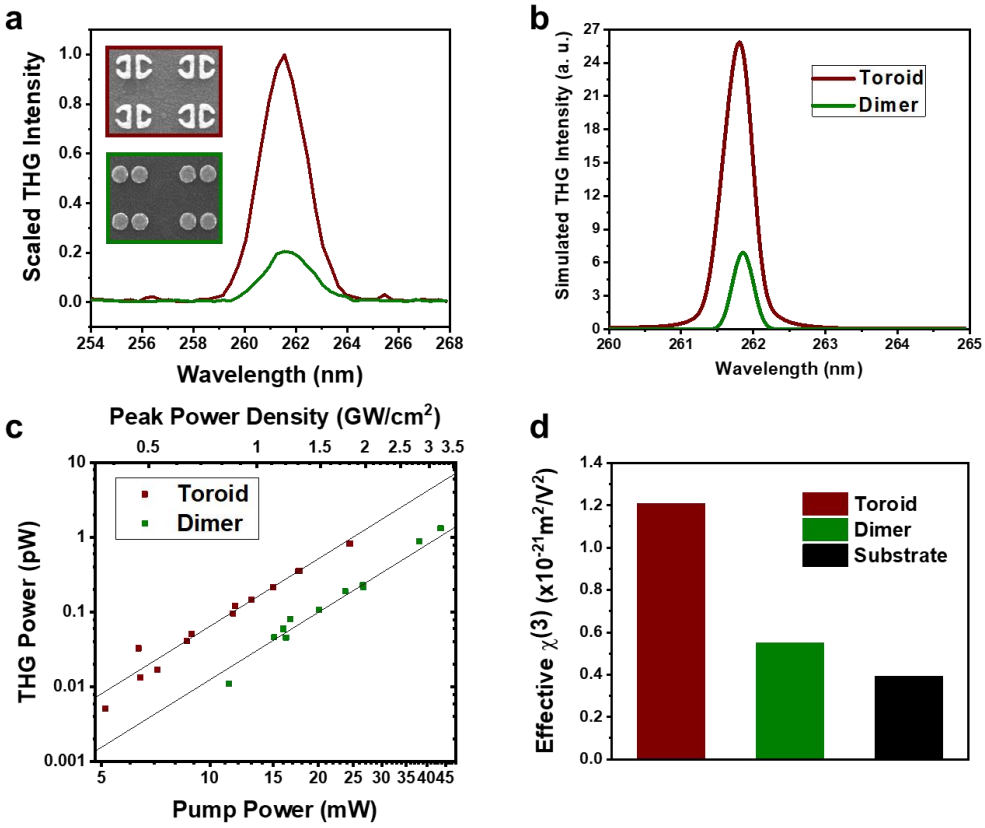

Figure 3. Nonlinear characterization. (a) Experimental and (b) simulated third harmonic spectrum of the toroidal metasurface (red) and dimer array (green). (c) Power dependence of the THG of the toroidal metasurface (red) and dimer array (green) with respect to the pump power in a log-log plot. The lines indicate a third order power dependence. (d) Comparison of the measured effective third order susceptibilities.

To probe the THG of the toroidal metasurface, we built a custom optical setup (Figure S3) using a CaF_2 lens to focus femtosecond laser pulses (~100 fs) onto the sample, with the light passing through the substrate first to avoid absorption of the generated UV signal in the glass substrate (see Figure S4 for a spectral measurement of the pump beam). The pump signal in the transmitted beam was routed through a deep UV filter, as well as a deep UV monochromator, and the THG was detected using a photomultiplier tube (PMT) (see Methods for details). The pump beam was polarized along the y axis. The generated third harmonic spectrum had a sharp peak centered around 262 nm (Figure 3a). In comparison, a disk-dimer array with a similar resonance position showed a much weaker THG response (about five times), given the same amount of Au per unit area (i.e. 13.5 % surface coverage, characterized by scanning electron microscopy and image processing). The average pump powers used were 27 mW for the toroid sample and 48 mW for the dimer sample. For comparison, the intensities in Figure 3a were scaled according to the calculated effective third order susceptibility values (see below). An experimental and simulated transmission spectrum of the dimer metasurface can be found in Figures S4 and S5, respectively.

The origin of the observed THG signal can indeed be attributed to THG generated in the metasurfaces, both by FDTD simulations (Figure 3b) and measurements of the power dependence (Figure 3c). The power measurements were conducted using the same optical setup as was used for the spectral measurements, except that the monochromator was replaced by additional UV filters to eliminate the pump signal. A log-log plot of the THG signal with respect to the excitation power of both structures follows the expected third order dependence. Notably, the signal intensity from the toroidal metasurface is nominally 5 times larger than the signal intensity due to the disk-dimer array. To further study the nonlinear efficiency, we calculated the effective third order susceptibility ($\chi_{eff}^{(3)}$) directly from the experimental data as[18,32,33]

$$\chi_{eff}^{(3)} = \frac{\varepsilon_0 c \lambda n_\omega w_0^2}{6 l P_\omega} \sqrt{\frac{n_\omega n_{3\omega} P_{3\omega}}{P_\omega}},$$

where ε_0 is the vacuum permittivity, c is the speed of light, λ is the wavelength of the fundamental harmonic, n_ω and $n_{3\omega}$ are the refractive indices at the fundamental (785 nm) and third (262 nm) harmonic frequency, w_0 is the beam waist radius, l is the interaction length, and P_ω and $P_{3\omega}$ are the peak powers at the fundamental and third harmonic, respectively (see Supporting Information for details). Figure 3d summarizes the effective nonlinear coefficient for the toroidal metasurface, the disk-dimer array and an un-patterned thick ITO film, for reference. An interaction length of 100nm, i.e. the ITO layer thickness, was chosen in each case. The $\chi^{(3)}_{eff}$(toroid) was found to be 1.2×10^{-21} m^2/V^2, 2.2- and 3.1-times greater than that of the disk-dimer array and the un-patterned substrate, respectively. This is consistent with previous works on ITO-plasmonic hybrid structures that have reported a higher THG of the hybrid structure compared to bare ITO crystals[23] or bare plasmonic structures[22-24]. However, a direct quantitative comparison between the THG enhancement in Ref. (22-24) is not applicable because of the different device geometry and excitation wavelength used in our work.

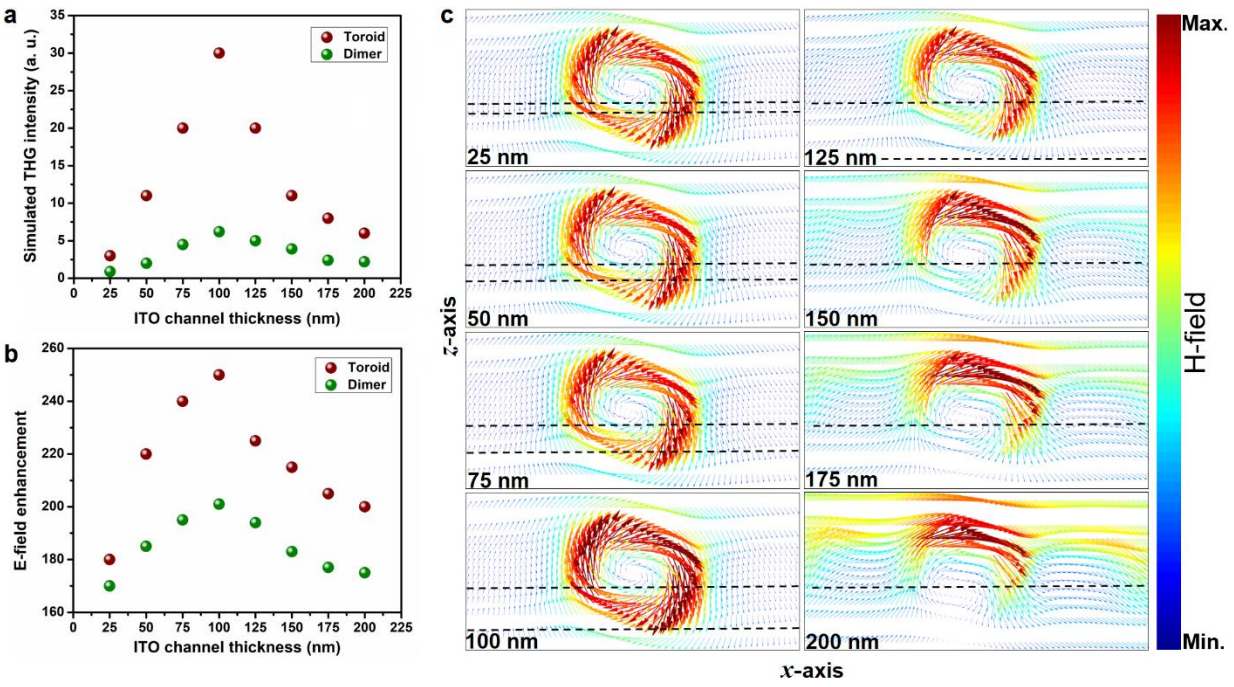

Figure 4. ITO thickness dependence. (a) Intensity of the THG signal and (b) the E-field enhancement calculated by integration across the whole metallic unit cell and ITO substrate at the pump frequency (785 nm) plotted as a function of ITO thickness for toroidal meta-atoms (in red) and disk-dimers (in green). (c) Cross-sectional (*xz*-plane) magnetic-field (H-field) vectorial map of the toroidal moment for a range of ITO sublayer thicknesses, from 25 nm to 200 nm.

Influence of ITO layer thickness. We also studied the influence of the ITO layer thickness on the intensity of the THG using FDTD simulations by integrating over the entire sublayer ITO channel (Figure 4a). The thickness of the ITO layer determines the effective refractive index in the structure, where most of the incident photonic power on the meta-atom is coupled into the channel underneath. In the proposed plasmonic meta-atom, the arisen magnetic hotspots strongly intensify the excitation of the toroidal dipolar moment by enhancing the spinning charge-current components. Therefore, we expect strong confinement of electromagnetic fields mostly inside the ITO layer, leading to boosting the generated harmonic signal. As shown explicitly in Figure 4b, increasing the thickness of the ITO layer from 25 nm to 100 nm gives rise to a strong increase in the intensity of the THG UV light. However, further increasing in the ITO thickness (>100 nm) sharply reduce the intensity. This trend can be explained by the confinement of the electric field at the excitation wavelength. This is in agreement with the standard description of THG in which the nonlinear polarization is proportional to the cube of the electric field at the excitation wavelength.[18] The underlying reason for reaching a maximum intensity at an ITO layer thickness of 100 nm can be understood by taking a closer look at how the toroidal mode changes with varying sublayer thickness. Figure 4c illustrates the cross-sectional magnetic-field vectorial map of the toroidal mode for different ITO thicknesses. The rotating charge-current feature is significantly enhanced with increasing thickness of the ITO layer up to 100 nm, and then weakens substantially with further increased thickness, due to lower electromagnetic field confinement (also see Figure S6). As it can be observed from the linear process, the recorded intense THG emission from the toroidal unit cell majorly comes from the significant near-field enhancement and confinement of electromagnetic fields in the ITO channel. The enhanced toroidal dipole at the fundamental wavelength combined with the confined fields in the ITO sublayer produce the total nonlinear harmonic emission. On the other hand, the THG signal from the disk-dimer array shows a much weaker dependence on the ITO thickness due to the confinement of electromagnetic fields in the capacitive opening between nanodisks, but also reaches a maximum around 100 nm due to

constructive interference of the scattered waves.[34,35] However, even for thicknesses outside the optimal value, the toroidal metasurface clearly outperforms the dimer array.

Discussion

We have demonstrated that a toroidal plasmonic metasurface on top an ITO layer dramatically boosts THG within that layer. The unique field enhancements of the toroidal structure, when combined with a sublayer with a strong nonlinear susceptibility, are responsible for the large increases in THG we have observed. The THG produced by the toroidal metasurface is about five times greater than that of a conventional disk-dimer array, and ten times greater than the un-patterned substrate. The strength of the THG signal depends strongly on the ITO layer thickness, indicating the importance of matching the spatial extent of the toroidal mode with the thickness of the ITO layer to achieve maximum THG enhancement. This work clearly demonstrates how carefully designed plasmonic structures, when matched to a nonlinear material of the appropriate dimension, can give rise to new hybrid metallodielectric media for frequency generation in neglected regions of the electromagnetic spectrum.

Methods

Simulations. We performed a set of simulations based on both finite-time-domain (FDTD, Lumerical 2018b) and finite element methods (FEM, COMSOL Multiphysics 5.3a), to precisely define the spectral response of the proposed meta-atom as well as the plasmonic dimer. The size of the spatial grids in all axes was set to 1.5 nm and periodic boundaries were employed to resemble a plasmonic metasurface. The Courant stability factor (~0.99) for the utilized model was achieved by setting the simulation time steps to dt = 0.0199 fs.[33] The incident beam was a regular plane-wave with a pulse length of 100 fs. The current density profile was computed by applying a Divergence Current analysis module based on implementing the effective permittivity of the system ($\vec{\boldsymbol{D}} = \boldsymbol{\varepsilon_{eff}}\vec{\boldsymbol{E}}$). Thus, the current density was solved in FDTD simulations via the following equation: $\vec{\boldsymbol{J}} = -\boldsymbol{i\omega}\left(\boldsymbol{\varepsilon_{ff}} - \boldsymbol{\varepsilon_0}\right)\vec{\boldsymbol{E}}$. More precisely, in our numerical analysis,

the relationship between the electric and displacement fields is introduced by: $\vec{\boldsymbol{D}}(\boldsymbol{\omega}) = \boldsymbol{\varepsilon_0}\boldsymbol{\varepsilon_r}(\boldsymbol{\omega}, \boldsymbol{dt})\vec{\boldsymbol{E}}(\boldsymbol{\omega})$. When *dt* tends to zero: $\lim_{\boldsymbol{dt}\to\boldsymbol{0}} \boldsymbol{\varepsilon_r}(\boldsymbol{\omega}, \boldsymbol{dt}) = \boldsymbol{n^2}(\boldsymbol{\omega})$, where $n(\boldsymbol{\omega})$ is the frequency-dependent refractive index obtained by our written code in the program. The E-field map (in Figure 2c) for the charge plot was generated by implementing Gauss's theorem in FEM analysis. To model the structures, we used Au dielectric permittivity values obtained empirically by Johnson and Christy.[37] The refractive index data for the ITO layer was adopted from Ref. 38. The nonlinear response of the studied structures was modelled using an FDTD approach by solving the corresponding Maxwell's equations and introducing ITO as a material with an exotic nonlinear susceptibility ($\boldsymbol{\chi^{(3)}}$) value.[29] Then, we excited the structure with a beam centered on the fundamental wavelength with ±5 nm span. The obtained resonance wavelength in the linear electromagnetic simulations was used as a source wavelength to obtain the THG (fundamental wavelength). Simplifying the induced nonlinear polarization components at the generated DUV signal, following relation was used: $\boldsymbol{P^{(3)}} = \boldsymbol{\varepsilon_0}\boldsymbol{\chi^{(3)}}\boldsymbol{E_j}(\boldsymbol{E}.\boldsymbol{E})$, where ε_0 is the permittivity of vacuum, E_i is a component of the electric field **E**, and *j* is the component in three axis directions. In the equation above, the E-field value as the near-field intensity was obtained by integration over the toroidal unit cell and the ITO sublayer. In the simulations, the metasurface consists of an infinite number of planar artificial scatterers in both the *x*- and *y*-direction. Correspondingly, the projected toroidal momentum normal to the incidence axis (z-axis) was defined using: $\mathbf{T} - (\mathbf{T}.\hat{\mathbf{r}})\hat{\mathbf{r}} = \boldsymbol{T_x}\hat{\boldsymbol{x}} + \boldsymbol{T_y}\hat{\mathbf{y}}$.[39]

Fabrication. All solvents were purchased from Sigma-Aldrich and used without further purification. ITO/glass substrates (obtained from a commercial supplier called Ossila) were rinsed with acetone while sonicating for 5 min and then rinsed with isopropanol (IPA) before use. The substrate was then spin-coated with poly(methyl methacrylate) (950 PMMA A2, MicroChem), and baked on a hot plate at 180 ℃ for 3 min. Subsequently, the nanostructures were patterned using a FEI Quanta 650 SEM with Nanometer Pattern Generation System (NPGS) software. A beam voltage of 30 kV, a beam current of 40 pA and a working distance of 7 mm were used. Then the substrate was developed in 1:3 methyl isobutyl ketone (MIBK) / IPA

for 50 s. Following development, 2 nm of titanium and 50 nm gold were deposited using e-beam evaporation. Liftoff was performed in acetone for 1 hr. Finally, the nanostructures were coated with a layer of 50 nm alumina using Atomic Layer Deposition (ALD) followed by a second layer of alumina (250 nm) using e-beam evaporation.

Linear Measurements. The linear transmission measurements were performed using an inverted Zeiss microscope (Axiovert 200 MAT) coupled with a spectrometer consisting of a monochromator (Princeton Instruments, Acton SP2150) and a charge-coupled device (CCD, Princeton Instruments, Pixis 400). A microscope illuminator (HAL 100) was used as an excitation source. The sample was illuminated glass-side first. The polarization was selected using a broad band wire gird polarizer (Thorlabs WP25M-UB). The transmission spectrum of the metasurface was retrieved by dividing the signal from the metasurface by the adjacent un-pattered area, consisting of the glass substrate, and the ITO and alumina layers.

Nonlinear Optical Measurements. The nonlinear optical measurements were performed using an ultrafast laser system (Coherent Mira 900, see the schematic in Figure S3). The center wavelength position was 785 nm and the pulse repetition rate was 76 MHz. The ultrafast pulses have a temporal width of about 100.6 fs. The laser was focused onto the sample via a CaF_2 lens (75 mm focal length). Similar to the linear measurements, the light passed through the substrate first. The incident peak power density on the sample ranged between 0.4 and 3.5 GW/cm^2 with a spot size of ~177 μm^2 (7.5 μm beam waist radius). The peak power density was estimated based on the spot size, the pulse width, and the repetition rate of the laser. The transmitted light was then collected with two CaF_2 lenses (40 mm focal length each). For the power measurements, the output beam was directly passed through several UV bandpass filters to eliminate the pump signal and detected with a PMT (Thorlabs PMTSS). For the spectral measurements, the output beam was routed through a UV bandpass filter as well as a UV monochromator (Thermo Jarrel Ash, 2400 grooves/mm grating) and detected with a PMT (ADIT Electron Tubes, 9781B6019).

Supporting information

Electric field maps, third harmonic measurements and data analysis, additional characterizations of the metasurfaces, and magnetic-field enhancement in the toroidal unit cell.

Author information

Corresponding Author

Email: halas@rice.edu

ORCID

Arash Ahmadivand: 0000-0003-0808-8775

Michael Semmlinger: 0000-0001-5430-733X

Liangliang Dong: 0000-0003-3848-1439

Burak Gerislioglu: 0000-0001-8575-7990

Peter Nordlander: 0000-0002-1633-2937

Naomi Halas: 0000-0002-8461-8494

Author Contributions

A.A., M.S. and L.D. contributed equally to this work. N.J.H. conceived the project. A.A., M.S. and L.D. designed the samples. A.A. performed the theoretical simulations. L.D. fabricated the samples. M.S. performed the optical measurements. B.G. assisted in the theoretical simulation. A.A., M.S. and L.D. analyzed the results and contributed to the preparation of the manuscript and discussions. P.J.N and N.J.H. supervised the research.

The authors declare no competing financial interest.

Acknowledgements

We gratefully acknowledge support from the Robert A. Welch Foundation, C-1220 (N.J.H) and C-1222 (P.N.), the National Science Foundation (NSF) under grant ECCS-1610229 (N.J.H. + P.N.), the Air Force Office of Scientific Research Multidisciplinary Research Program of the University Research Initiative (AFOSR MURI FA9550-15-1-0022) (N.J.H. + P.N.), and the Defense Threat Reduction Agency (HDTRA1-16-1-0042) (N.J.H. + P.N.). We thank Kyle Chapkin for characterizing the temporal pulse width of the ultrafast laser and thank Ben Cerjan and Dr. Chao Zhang for their support and all the useful discussions we had with them.

TOC Art

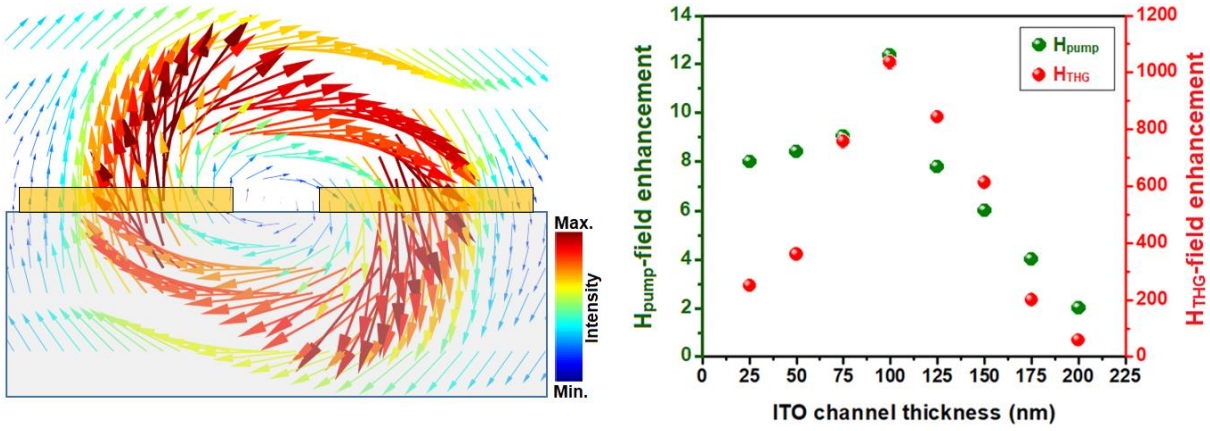

References

(1) Mesch, M.; Metzger, B.; Hentschel, M.; Giessen, H. Nonlinear Plasmonic Sensing. *Nano Lett.* **2016**, *16*(5), 3155–3159.

(2) Butet, J.; Martin, O. J. F. Nonlinear Plasmonic Nanorulers. *ACS Nano* **2014**, *8*(5), 4931–4939.

(3) Weigelin, B.; Bakker, G. -J.; Friedl, P. Third Harmonic Generation Microscopy of Cells and Tissue Organization. *J. Cell Sci.* **2016**, *129*(2), 245–255.

(4) Sidiropoulos, T. P. H.; Röder, R.; Geburt, S.; Hess, O.; Maier, S. A.; Ronning, C.; Oulton, R. F. Ultrafast Plasmonic Nanowire Lasers near the Surface Plasmon Frequency. *Nat. Phys.* **2014**, *10*(11), 870–876.

(5) Oulton, R. F.; Sorger, V. J.; Zentgraf, T.; Ma, R. M.; Gladden, C.; Dai, L.; Bartal, G.; Zhang, X. Plasmon Lasers at Deep Subwavelength Scale. *Nature* **2009**, *461*(7264), 629–632.

(6) Zhang, Y.; Manjavacas, A.; Hogan, N. J.; Zhou, L.; Ayala-Orozco, C.; Dong, L.; Day, J. K.; Nordlander, P.; Halas, N. J. Toward Surface Plasmon-Enhanced Optical Parametric Amplification (SPOPA) with Engineered Nanoparticles: A Nanoscale Tunable Infrared Source. *Nano Lett.* **2016**, *16*(5), 3373–3378.

(7) Klein, M. W.; Wegener, M.; Feth, N.; Linden, S. Experiments on Second-and Third-Harmonic Generation from Magnetic Metamaterials. *Opt. Express* **2007**, *15*(8), 5238–5247.

(8) Soavi, G.; Wang, G.; Rostami, H.; Purdie, D. G.; De Fazio, D.; Ma, T.; Luo, B.; Wang, J.; Ott, A. K.; Yoon, D.; Bourelle S. A. Broadband, Electrically Tunable Third-Harmonic Generation in Graphene. *Nat. Nanotechnol.* **2018**, *13*(7), 583–588.

(9) Yang, Y.; Wang, W.; Boulesbaa, A.; Kravchenko, I. I.; Briggs, D. P.; Puretzky, A.; Geohegan, D.; Valentine, J. Nonlinear Fano-Resonant Dielectric Metasurfaces. *Nano Lett.* **2015**, *15*(11), 7388–7393.

(10) Levy, J. S.; Foster, M. A.; Gaeta, A. L.; Lipson, M. Harmonic generation in silicon nitride ring resonators, *Opt. Express* **2011**, *19*(12), 11415-11421.

(11) Monat, C.; Grillet, C.; Collins, M.; Clark, A.; Schroeder, J.; Xiong, C.; Li, J.; O'faolain, L.; Krauss, T. F.; Eggleton, B. J.; Moss, D. J. Integrated optical auto-correlator based on third-harmonic generation in a silicon photonic crystal waveguide. *Nat. Commun.* **2014**, 5, 3246.

(12) Lassiter, J. B.; Chen, X.; Liu, X.; Ciracì, C.; Hoang, T. B.; Larouche, S.; Oh, S. H.; Mikkelsen, M. H.; Smith, D. R. Third-Harmonic Generation Enhancement by Film-Coupled Plasmonic Stripe Resonators. *ACS Photonics* **2014**, *1*(11), 1212–1217.

(13) Hentschel, M.; Utikal, T.; Giessen, H.; Lippitz, M.; Quantitative modeling of the third harmonic emission spectrum of plasmonic nanoantennas. *Nano Lett.* **2012**, *12*(7), 3778-3782.

(14) Li, G. X.; Li, T.; Liu, H.; Li, K. F.; Wang, S. M.; Zhu, S. N.; Cheah, K. W. Spectral analysis of enhanced third harmonic generation from plasmonic excitations. *Appl. Phys. Lett.* **2011**, *98*(26), 261909.

(15) Ahmadivand, A.; Gerislioglu, B.; Pala, N. Optothermally Controllable Multiple High-Order Harmonics Generation by Ge2Sb2Te5-Mediated Fano Clusters. *Opt. Mater.* **2018**, *84*, 301–306.

(16) Cox, J. D.; Marini, A.; De Abajo, F. J. G. Plasmon-Assisted High-Harmonic Generation in Graphene. *Nat. Commun.* **2017**, *8*, 14380.

(17) Shibanuma, T.; Grinblat, G.; Albella, P.; Maier, S. A. Efficient Third Harmonic Generation from Metal-Dielectric Hybrid Nanoantennas. *Nano Lett.* **2017**, *17*(4), 2647–2651.

(18) Reintjes, J. F. *Nonlinear Optical Parametric Processes in Liquids and Gases*, 1st ed.; Academic Press, 1984.

(19) Kauranen, M.; Zayats, A. V. Nonlinear Plasmonics. *Nat. Photonics* **2012**, *6*, 737-748.

(20) Metzger, B.; Schumacher, T.; Hentschel, M.; Lippitz, M.; Giessen, H. Third Harmonic Mechanism in Complex Plasmonic Fano Structures. *ACS Photonics* **2014**, *1*(6), 471–476.

(21) Walsh, G. F.; Dal Negro, L. Enhanced Second Harmonic Generation by Photonic-Plasmonic Fano-Type Coupling in Nanoplasmonic Arrays. *Nano Lett.* **2013**, *13*(7), 3111–3117.

(22) Metzger, B.; Hentschel, M.; Schumacher, T.; Lippitz, M.; Ye, X.; Murray, C. B.; Knabe, B.; Buse,

K.; Giessen, H. Doubling the Efficiency of Third Harmonic Generation by Positioning ITO Nanocrystals into the Hot-Spot of Plasmonic Gap-Antennas. *Nano Lett*. **2014**, *14*(5), 2867–2872.
(23) Aouani, H.; Rahmani, M.; Navarro-Cía, M.; Maier, S. A. Third-Harmonic-Upconversion Enhancement from a Single Semiconductor Nanoparticle Coupled to a Plasmonic Antenna. *Nat. Nanotechnol*. **2014**, *9*(4), 290–294.
(24) Aouani, H.; Navarro-Cía, M.; Rahmani, M.; Maier, S. A. Unveiling the Origin of Third Harmonic Generation in Hybrid ITO-Plasmonic Crystals. Adv. *Opt. Mater*. **2015**, *3*(8), 1059–1065.
(25) Grinblat, G.; Li, Y.; Nielsen, M. P.; Oulton, R. F.; Maier, S. A. Efficient Third Harmonic Generation and Nonlinear Subwavelength Imaging at a Higher-Order Anapole Mode in a Single Germanium Nanodisk. *ACS Nano* **2017**, *11*(1), 953–960.
(26) Grinblat, G.; Li, Y.; Nielsen, M. P.; Oulton, R. F.; Maier, S. A. Enhanced Third Harmonic Generation in Single Germanium Nanodisks Excited at the Anapole Mode. *Nano Lett.* **2016**, *16*(7), 4635–4640.
(27) Papasimakis, N.; Fedotov, V. A.; Savinov, V.; Raybould, T. A.; Zheludev, N. I. Electromagnetic Toroidal Excitations in Matter and Free Space. *Nat. Mater.* **2016**, *15*(3), 263–271.
(28) Nordlander, P. Plasmonics: The Dark Side of the Ring. *Nat. Nanotechnol.* **2013**, *8*(2), 76–77.
(29). Humphrey, J. L.; Kuciauskas, D. Optical susceptibilities of supported indium tin oxide thin films. *J. Appl. Phys.* **2006**, *100*(11), 113123.
(30) Kruk, S.; Weismann, M.; Bykov, A. Y.; Mamonov, E. A.; Kolmychek, I. A.; Murzina, T.; Panoiu, N. C.; Neshev, D. N.; Kivshar, Y. S. Enhanced Magnetic Second-Harmonic Generation from Resonant Metasurfaces. *ACS Photonics* **2015**, *2*(8), 1007–1012.
(31) Wang, L.; Shorokhov, A. S.; Melentiev, P. N.; Kruk, S.; Decker, M.; Helgert, C.; Setzpfandt, F.; Fedyanin, A. A.; Kivshar, Y. S.; Neshev, D. N. Multipolar Third-Harmonic Generation in Fishnet Metamaterials. *ACS Photonics* **2016**, *3*(8), 1494–1499.
(32) Boyd, R. W. *Nonlinear Optics*, 2nd ed.; Academic Press, 2003.
(33) Sergey A. Ponomarenko. *Fundamentals of Nonlinear Optics*; Dalhousie University, 2012.
(34) Ahmed, A.; Gordon, R. Single Molecule Directivity Enhanced Raman Scattering Using Nanoantennas. *Nano Lett.* **2012**, *12*(5), 2625–2630.
(35) Wang, D.; Zhu, W.; Best, M. D.; Camden, J. P.; Crozier, K. B. Directional Raman Scattering from Single Molecules in the Feed Gaps of Optical Antennas. *Nano Lett.* **2013**, *13*(5), 2194–2198.
(36) Zheng, F.; Chen, Z. Numerical Dispersion Analysis of the Unconditionally Stable 3-D ADI-FDTD Method. *IEEE Trans. Microw. Theory Tech.* **2001**, *49*(5), 1006–1009.
(37) Johnson, P. B.; Christy, R. W. Optical Constants of the Noble Metals. *Phys. Rev. B* **1972**, *6*(12), 4370–4379.
(38) König, T. A. F.; Ledin, P. A.; Kerszulis, J.; Mahmoud, M. A.; El-Sayed, M. A.; Reynolds, J. R.; Tsukruk, V. V. Electrically Tunable Plasmonic Behavior of Nanocube-Polymer Nanomaterials Induced by a Redox-Active Electrochromic Polymer. *ACS Nano* **2014**, *8*(6), 6182–6192.
(39) Gerislioglu, B.; Ahmadivand, A.; Pala, N. Tunable Plasmonic Toroidal Terahertz Metamodulator. *Phys. Rev. B* **2018**, *97*(16), 161405.